Modeling, simulation and experimental validation of solid media in capacitive wireless power transfer

, , ,

Modelling, Simulation and Experimental Validation of Solid Media in Capacitive Wireless Power Transfer

Cédric Lecluyse[a], Arman Ghaderi Baayeh[a], Ben Minnaert[b], Michael Kleemann[a]

[a]KU Leuven Faculty of Engineering Technology Ghent Technology Campus, Department of Electrical engineering (ESAT)
[b] University of Antwerp, Cosys-Lab

Abstract

Capacitive wireless power transfer (CPT) employs an electric field to transmit energy through a medium. Air is the most often used and a well-understood medium. However, CPT can also bridge other solid media and even benefit from them as the dielectric properties of the medium govern the strength of the capacitive coupling. The parasitic elements of the coupling are influenced by the medium, in particular the leakage resistance. In this work, an analytical model is proposed that quantifies the leakage resistance losses in CPT systems for media. The model is validated by both finite element simulations and experiments on three different media: air, plexiglass and polytetrafluorideethylene (PTFE). As a result, at 1 MHz, the leakage resistance of plexiglass is 6 times higher than that of air while that of PTFE is 1.7 times smaller. This proves that a material with a large dipole moment generates larger losses in the medium which negatively affect system efficiency.

Keywords: Capacitive wireless power transfer, Dielectric materials, Leakage resistance, Dipole moment

1. Introduction

Wireless power transfer (WPT) is self-descriptive: transferring power without a wire. In 1891, Nikola Tesla showcased the concept of WPT by illuminating a light bulb using an alternating field between two plates. This pioneering demonstration is nowadays referred to as wireless capacitive power transfer. Despite CPT being the first WPT technology presented, most research has been conducted on inductive wireless power transfer (IPT). This is because of the ease with which it can be implemented, as a few kilohertz is enough to drive the transmission coil. Furthermore, it is able to transfer powers of several kW at efficiencies of 95 % without operating at hazardous voltages [1, 2]. The relative ease of use and efficiency, makes it now the most widely used WPT technology. However, CPT has some advantages over IPT. It is able to transfer energy with metal objects nearby and emits less electromagnetic interference (EMI). Moreover, it more tolerant to misalignment and is the coupler is cheaper to manufacture and more compact [3, 4].

The first relevant CPT system was demonstrated in 2008 [5]. Here, a CPT system charges a robot with an efficiency of 44 % at a distance of 3 mm with a power of 40 W. From this point on, research on the inverter, compensation networks and the coupler enabled the transmission of powers from milliwatts to kilowatts over distances from millimeters to tens of centimeters [3, 4].

The major challenge for CPT is the low coupling capacitance which ranges from pF to nF. To increase the power, the frequency or the magnitude of the voltage needs to increase. For this reason, research has been done on the inverter of the CPT that drive the transfer plates with several 100 kHz [6–8]. Additionally, power levels can be increased with compensation networks. These networks consisting of inductors and capacitors have been demonstrated for CPT systems up to 3.75 kW for distances up to 15 cm, with alternating frequencies of up to 27.12 MHz [9–13]. However, these networks also have the disadvantage of making the system more difficult to design and increase the total volume of the CPT system significantly. Finally, the power level can be increased by using a medium other than air between the plates. On the one hand, the dielectric properties of the medium increase the strength of the capacitive coupling between the primary and secondary side. On the other hand, the losses in the medium deteriorate the efficiency.

In the literature, studies can be found on dielectric properties of water or skin and their behavior in a CPT system. However, these kind of studies are limited to low power transfer of less than 130 W [14–17]. Despite the profound knowledge on dielectric materials for capacitors, to the best knowledge of the authors, little is known about media different from air for CPT applications with 100 W or more. Solid materials have been investigated for their dielectric properties for purposes other than capacitive power transfer. These investigations are often inapplicable for modeling a CPT system because they were performed in a frequency range above or below that of CPT which is between 500 kHz and 15 MHz [18–21]. Furthermore, finite element software such as CST Studio, COMSOL or ANSYS has data describing the dielectric properties of materials. This data is often obtained from a model such as the Debye-model and based on estimated parameters. However, it seems that this data is inaccurate and partly incomplete, neglecting for instance the losses in the materials. In addition, the data is also often only suitable for a frequency range outside that of CPT. Thus, there is a research gap between the dielectric properties of construction materials and their influence on the parasitic elements in a CPT system. By bridging this gap, more CPT applications become accessible. This is done in this paper with two contributions:

C1. It develops an extended pi model of the coupler regarding (solid) media

C2. It validates the model and it delivers experimental data on dielectric properties of construction materials

These contribution serve the following research questions: (1) How to model the dielectric properties of media for CPT applications? (2) How do solid media influence CPT? To provide answers on these questions the paper is divided into the following four sections. The following second section is about the fundamentals of the capacitive coupler and the effect of the medium on the coupling capacitance and the coupler losses. The third section develops a novel extended pi model (C1), based on fundamental principles of the CPT coupler. The fourth section validates this model with finite element simulations and experimental research for three media. This also yields experimental data on dielectric properties of materials in CPT applications (C2).
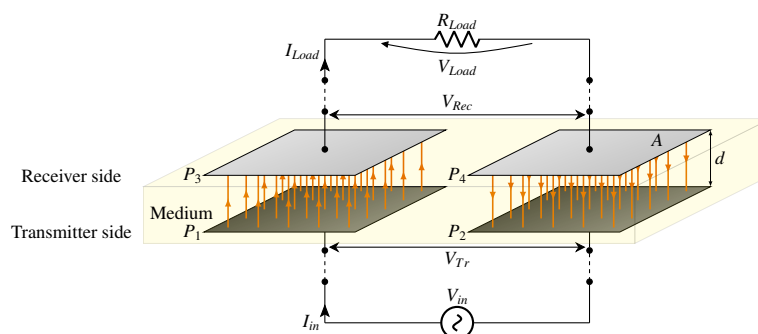

Figure 1: Four plate CPT coupler circuit

2. Capacitive power transfer model

A capacitive power transfer system as shown in 1, consists of four main components. The first component is the inverter, represented as voltage source V_{in}. The second, the dashed lines represent the recommended compensation network on transmitter and/or receiver side. These networks can go from the most simple series inductor to a complicated multiple stage LC-combination. The third, a coupler needed to transmit energy from transmitter to receiver side. Here, the most common coupler structure found in the literature is shown, the parallel four plate structure. The fourth component, the load, is represented as a resistance R_{load}. In practice the load includes a rectifier.

When considering the circuit in Figure 1, with the parallel four plate structure, a CPT system consists of two parallel plate capacitors. The strength of the coupling between transmitter and receiver side is determined by the main capacitances C_{13} between plates P_1 and P_3, and C_{24} between plates P_2 and P_4. Undesirable parasitic capacitances, cross-coupling C_{14} & C_{23} and leakage C_{12} & C_{34} capacitances, occur. These affect the coupling capacitance negatively. These six capacitances are often mapped to the pi model (Figure 2) using Equations (1) - (3) [22]. This model consists

2

of three capacitances: mutual capacitance C_m, primary capacitance C_p and secondary capacitance C_s. The larger the parasitic capacitances, the larger the primary and secondary capacitances are. This weakens the coupling between transmitter and receiver side. The pi model does not include parasitic elements such as the leakage resistance of the medium. Therefore, in the following section, the operation of a parallel plate capacitor is discussed in more detail.

$$C_p = \frac{(C_{13} + C_{14})(C_{23} + C_{24})}{C_{13} + C_{14} + C_{23} + C_{24}} \tag{1}$$

$$C_s = \frac{(C_{13} + C_{23})(C_{14} + C_{24})}{C_{13} + C_{14} + C_{23} + C_{24}} \tag{2}$$

$$C_m = \frac{C_{13} \cdot C_{24} - C_{14} \cdot C_{23}}{C_{13} + C_{14} + C_{23} + C_{24}} \tag{3}$$

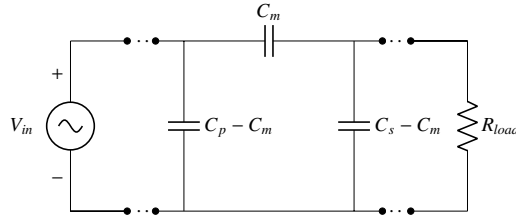Figure 2: Pi-model of CPT coupler

2.1. Lossy parallel plate capacitor

Losses in the pi model, which represent the CPT coupler, do not consist of parasitic elements such as the leakage resistance of the medium. As CPT systems typically operate frequencies between 500 kHz and 15 MHz, parasitic effects cannot be neglected. Losses occur in the medium and in the wiring. For this reason, the practical capacitor in Figure 3 is considered [23–25]. This equivalent circuit bears the following elements:

- The series capacitance C_{ser}, caused by the wires connected to the terminals of the plates.
- The series resistance R_{ser}, caused by the the resistance of the wires and connections.
- The series inductance L_{ser}, caused by the wires and plates.
- The parallel resistance R_{par}, caused by the dielectric medium between the coupler plates.
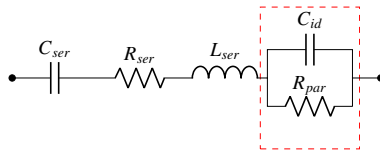- The ideal capacitance C_{id}, that is used in the pi model.

Figure 3: Lossy capacitor

3

To determine the influence of the medium, this paper focuses on R_{par} and C_{id}. These parameters are determined by the medium itself and are not directly affected by the cabling.

The parameters R_{par} and C_{id} have a significant influence on the power transfer between two metal plates. To achieve power transfer between two plates, an alternating voltage is applied to the plates. When an alternating field is applied, the dipoles in the medium align themselves to it as shown in Figure 4. This causes the capacitor to charge and discharge, which results in a polarization current [23, 26]. At higher frequencies than several hundred kHz, not every dipole fully aligns with the applied electric field. This causes friction between the dipoles and so dielectric loss. In this manner, the dielectric constant ϵ equals $\epsilon' - j \cdot \epsilon''$, with ϵ' the dielectric constant and ϵ'', the representation of how much the dielectric can be polarized. For instance, the capacitance for a parallel plate capacitor, with area A and distance d between the plates, is calculated with equation (4). Here C_0 denotes the vacuum capacitance.
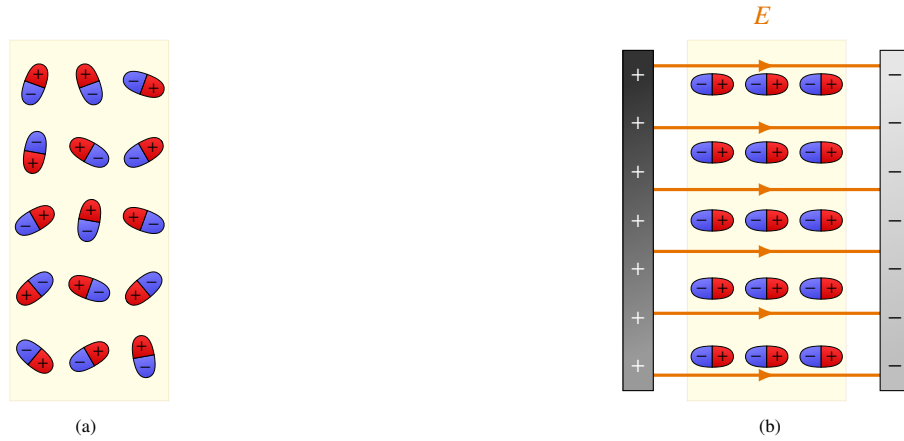

Figure 4: (a): Dielectric without plate capacitor; (b): Dipoles orientation of dielectric with plate capacitor

$$C = (\epsilon' - j \cdot \epsilon'') \cdot C_0 \text{ with } C_0 = \epsilon_0 \cdot \frac{A}{d} \tag{4}$$

The total impedance of the parallel plate capacitor Z_c becomes:

$$Z_c = \frac{1}{j \cdot \omega \cdot C} \tag{5}$$

$$= \frac{1}{j \cdot \omega \cdot (\epsilon' - j \cdot \epsilon'') \cdot C_0} \tag{6}$$

This impedance can be translated to the parallel connection of the capacitance C_{id} and R_{par} in Figure 3. Equations (7) and (8) yield the frequency-dependent reactance and resistance for that parallel connection.

$$X_{C_{id}} = \Im(Z_c) = \frac{1}{j \cdot \omega \cdot \epsilon' \cdot C_0} \Longrightarrow C_{id} = \epsilon' \cdot C_0 \tag{7}$$

$$R_{par} = \Re(Z_c) = \frac{1}{\omega \cdot \epsilon'' \cdot C_0} \tag{8}$$

As it is not feasible to measure the parallel equivalent of the coupler impedance, R_{par} is transformed to its series equivalent R_c.

$$R_c = \frac{\epsilon''}{\omega \cdot C_0 \cdot (\epsilon'^2 + \epsilon''^2)} \tag{9}$$

4

2.2. Leakage resistance of a CPT system

When an alternating voltage is applied across the plates of a CPT system, losses will occur in the medium. These losses are characterized by the leakage resistance. To determine the leakage resistance of the medium in a CPT system, the circuit with six impedances in Figure 5 is considered. The impedances comprise the coupling capacitance combined with the leakage resistance.
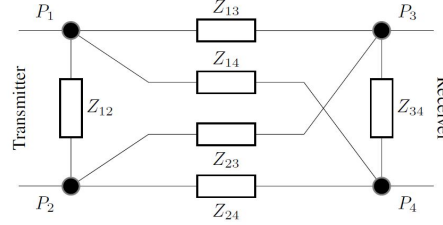

Figure 5: Detailed impedance model of the four plate CPT coupler

The CPT coupler is assumed to be symmetric. This means that the distance, between the plates is equal along their surfaces, the plates have identical sizes and the distance between the plates on the transmitter and receiver side is the same. As a result, Z_{13} to Z_{34} can be simplified with Equations(10) - (12).

$$Z_{13} = Z_{24} = Z_{main} \tag{10}$$

$$Z_{23} = Z_{14} = Z_{cross} \tag{11}$$

$$Z_{12} = Z_{34} = Z_{leak} \tag{12}$$

Based on these assumptions, the parameters of a new pi model (Figure 6), analogous to Figure 2, are found (full derivation described in the appendix).

$$Z_m = \frac{2 \cdot Z_{main} \cdot Z_{cross}}{Z_{main} - Z_{cross}} \tag{13}$$

$$Z_{tr} = \frac{Z_{leak} \cdot Z_{cross}}{Z_{leak} + Z_{cross}} \tag{14}$$

$$Z_{rcv} = \frac{Z_{leak} \cdot Z_{cross}}{Z_{leak} + Z_{cross}} \tag{15}$$

The cross coupling and leakage impedance, Z_{cross} and Z_{leak} can be neglected when the distance between the transmitter and receiver is smaller than 25 mm [27]. At this distance the parasitic impedances are significantly larger than the main impedance Z_{main}, and so are Z_{tr} and Z_{rcv} significantly larger than Z_m. This means that the pi model is reduced to the mutual impedance Z_m. This is equal to twice the main impedance according to Equation (13). This implies that the coupler can be described by two parallel plate capacitors in series. The total impedance of the CPT coupler, according to the Equations (7) and (9), is given by Equation (17).

$$Z_m = 2 \cdot Z_{main} = 2 \cdot R_c - 2 \cdot j \cdot X_{c_{id}} \tag{16}$$

$$= 2 \cdot \frac{\epsilon''}{\omega \cdot C_0 \cdot (\epsilon'^2 + \epsilon''^2)} - 2 \cdot \frac{j}{\omega \cdot \epsilon' \cdot C_0} \tag{17}$$

3. Parameter estimation of the CPT coupler via simulations

The extend pi model is validated in finite element (FE) software. The simulations are implemented in CST Studio based on the model in Figure 7. The model consists of four identical square (300 mm by 300 mm) coupler plates (in
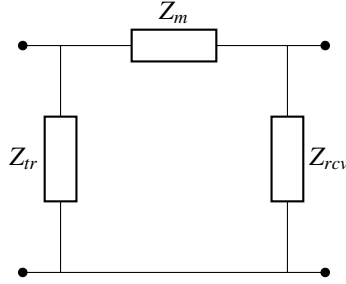
Figure 6: New pi model of CPT coupler

black), 2 mm thick. An overview of the CPT coupler specifications used in the simulation is given in Table 1. The medium (in white) is 5 mm thick. The two triangles (in red) indicate the ports of the two-port network (Figure A.11) to which the model can be mapped. According to this, the main impedance is calculated in Y_{21}. Based on Equation (17), the capacitance and parasitic resistance of the coupler is determined via FE simulations. These results allows to validate the assumptions made in the previous section with FE simulation and measurements.
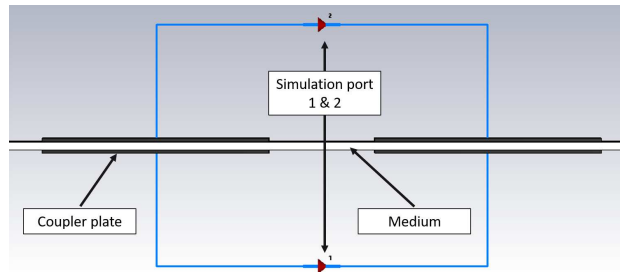

Figure 7: CST Studio model of a four plate structure system

Table 1: CPT coupler simulation specifications

Specification	
Plate size	300 mm by 300 mm
Plate thickness	2 mm
Medium thickness	5 mm
Medium material	Air / Plexiglass / PTFE
Frequency range	400 kHz - 10 MHz

To validate the influence of the dielectric properties of a medium on the leakage resistance and coupler capacitance, three different media are compared with each other. The first material is air which is commonly used as a medium in literature and is assumed to have no dipole moment. The second medium measured, is polymethyl methacrylate (PMMA) or plexiglass. As a third medium polytetrafluorideethylene (PTFE), which is often used a wire insulation, is measured. This material is included in this paper as it can be found in literature that no dipole moment is present in the molecules [28, 29]. As no practical dielectric properties are available in the FE software for these materials, the complex permittivity of the materials is measured with the measuring set-up explained in the next section.

Equations (18) and (19) describe how the complex permittivity $\epsilon = \epsilon' - j \cdot \epsilon''$ is determined. Parameters C_{id} and R_{meas} are measured with the set-up, shown in Figure 9a, while the vacuum capacitance C_0 is obtained through FE simulations. By applying the measured permittivity values to the FE-model, the mutual impedance Z_m is determined by
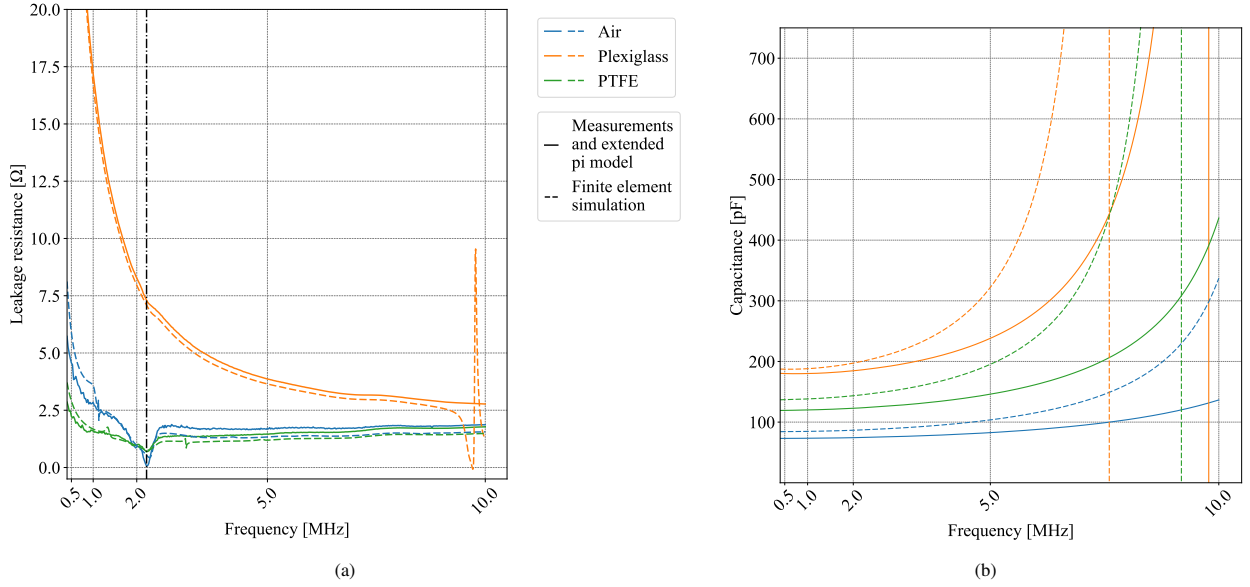
Figure 8: (a) Leakage resistance and (b) capacitance measurement/FE simulations of the CPT coupler for media air, plexiglass and PTFE.

the Y parameters obtained from the simulation. The result is an array of complex numbers, whose real part represents the leakage resistance and the imaginary part is related to the coupler capacitance. The results are interpreted by using Equation (16). The FE simulations are plotted as dashed lines in Figure 8.

$$C_{id} = \epsilon' \cdot C_0 \implies \epsilon' = \frac{C_{id}}{C_0} \tag{18}$$

$$\tan\theta = \frac{R_{meas}}{\frac{1}{\omega \cdot C_{id}}} = \frac{\epsilon''}{\epsilon'} \implies \epsilon'' = \frac{R_{meas}}{\frac{1}{\omega \cdot C_{id}}} \cdot \epsilon' \tag{19}$$

The extended pi model developed in section 2 and the findings from the FE simulations in section 3 are validated with the laboratory set up shown in Figure 9a. An overview of the set-up is given in Fig 9b [30]. The set-up consists of a height-adjustable platform that allows to alter the distance between transmitter and receiver. Two stepper-motors move this platform with an accuracy of ± 0.1 mm. For the measurements in this paper, the platform distance is fixed so that the distance between the transmitter and receiver is 5 mm. The stepper motors are programmatically controlled so that the experiments can be automated. An impedance analyzer, Wayne Kerr 6500, measures the capacitance and leakage resistance of the CPT coupler. This device obtains the CPT's impedance in the frequency range from 400 kHz to 10 MHz which is typically used in CPT [3]. This device has an accuracy of 0.05 %. All components of the set-up work together via a Python script that generates a CSV file with all the measurements at the end [30].

Each medium fills the 5 mm wide void between the 300 mm by 300 mm coupler plates, as shown in Fig 10. At the time of measurement, the humidity in the room is 40% and the temperature 22.4 °C. Figure 8a shows the results of the leakage resistance FE simulations (dashed lines) and measurements (full lines). An overview of the leakage resistances of the three media at 1 MHz is given in Table 2.

Four main observations are possible from this figure. First, calculating the leakage resistance with the extended pi model in Equation (17) yields three curves that matches the measurements. No deviation is visible, the extended pi model yields the leakage resistance with an accuracy of 0.05 % or better for the given set-up. At higher frequencies, from 5 MHz on, the deviation is approximately 20% and is presumably from an inaccuracy of the simulation model. From this it can be further concluded that the parasitic elements such as the cross-coupling and leakage impedance do not affect the leakage resistance.

Second, the figure shows that there is a leakage resistance present for air. At a frequency of 1 MHz, this is 2.84 Ω and thus not negligible. As the humidity of the room was 40 %, the leakage resistance of air is probably caused
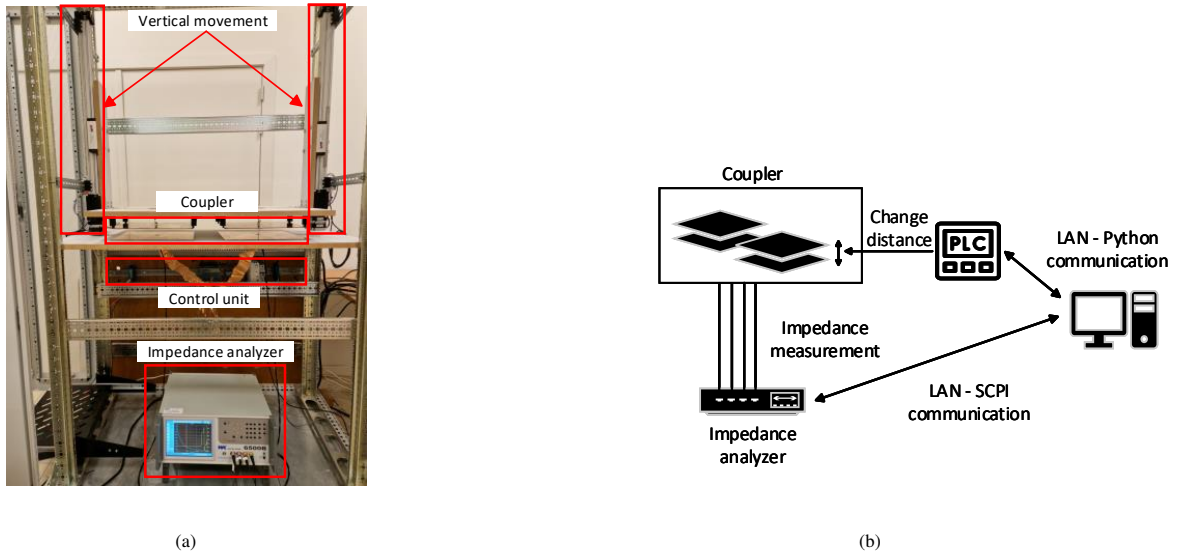
7

Figure 9: (a):Practical set-up of CPT impedance measurements; (b):Block diagram of the practical set-up

by the presence if water in the air. Water has a high permittivity, this for both the real ($\epsilon' = 80$) and imaginary part ($\epsilon'' = 0.12$) [31, 32]. The higher the humidity, the higher the leakage resistance will be. Further, the leakage resistance for air shows a dip at 2.3 MHz, see Figure 8a. This is probably due to the dielectric properties of one of the components present in air.

Third, a leakage resistance is measured for PTFE. At a frequency of 1 MHz, this is 1.61 Ω. Presence of dielectric losses is caused by impurities in the material and the presence of a thin layer, less than 0.5 mm, of air between the medium and the plates. Despite the fact that the loss tangent of the material increases, the leakage resistance decreases with the increasing frequency. For PTFE, also a dip is noticed at 2.3 MHz. This caused by the presence of a thin layer of air between the plates and the medium, since it occurs at the same frequency as the dip in air.

Fourth, the leakage resistance measured for plexiglass is much higher than for air and PTFE. At a frequency of 1 MHz, this is 17.89 Ω, which is about 6 times higher than air and 11 times higher than the leakage resistance of PTFE. This is due to the molecular structure of plexiglass, which is not as symmetrical as PTFE. This asymmetrical structure causes a dimolle moment of 1.4 D at 10 kHZ while PTFE has a relatively small dipole moment above several GHz [33, 34].

In Figure 8b the FE simulation (dashed lines) and measurements (full lines) are plotted for the coupler capacitance. Table 2 gives an overview of the measurement and simulation results for the coupler capacitance at 1 MHz. As expected, the capacitance increases as the permittivity increases combined with an increasing frequency. Further it can be concluded that for frequencies up to 2 MHz, the resulting capacitance of the FE simulations describes the measurement with a typical deviation of 15%. For higher frequencies, the deviation increases. The deviations between

Table 2: CPT coupler measurement & simulation results at 1 MHz

Medium	Leakage resistance R_c [Ω] (simulation)	Coupler capacitance C_{id} [pF] (simulation)
Air	2.84 (3.55)	73.4 (84.6)
Plexiglass	17.2 (16.6)	180 (188)
PTFE	1.61 (1.67)	120 (138)

8

measurements and simulations can be explained by additional parasitic couplings in practice. These are not included in the simulations as they assume ideal conditions. This is probably also the reason why the deviation increases above 2 MHz when the parasitic couplings become stronger. No plot of the capacitance obtained from Equation (17) is included as the real part of the permittivity was determined from the measurements using this equation.
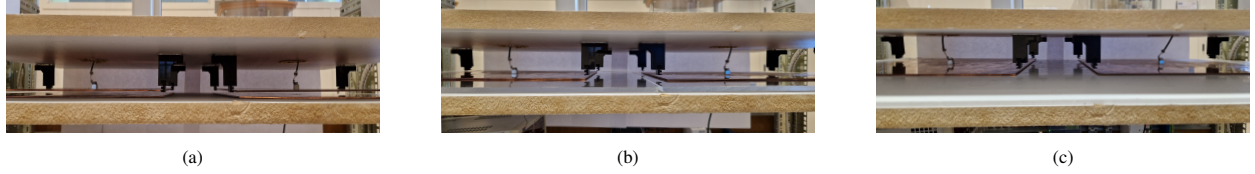

(a)   (b)   (c)

Figure 10: CPT coupler with (a) air, (b) plexiglass and (c) PTFE as medium.

4. Conclusion

An extended pi model for capacitive wireless power transfer (CPT) systems has been proposed that takes into account the dielectric properties of solid media. Exceeding the state of research, the model reflect the frequency-dependent permittivity and losses in media. The model was first validated against commercial finite element simulations which yielded deviations of 15% to 20%. The model was then validated in experiment, using air, plexiglass and polytetrafluorideethylene (PTFE) as media. The experiment testified that the extended model has an error of less than 5%. Hence, for the selected media, the proposed extended pi model is superior to FEM simulations.

Additionally, the measurements showed that a medium causes an increase in coupler capacitance. In comparison to air, plexiglass and PTFE increase the capacitance by factor 2.45 and 1.63. Also, the experiment confirmed that the medium's dipole moment governs the losses in a CPT application. To further explore the application opportunities of CPT, more dielectric data on solid media such as wood, bricks or polyurethane should be measured within the frequency range, 500 kHz to 20 MHz, of capacitive power transfer. Furthermore, the outcomes should be further validated in an experimental CPT set-up through electrical quantities.

Appendix A. Elaboration of two-port networks of a CPT coupler

In this appendix the complete elaboration of the two-port networks in Section 2 is given.

The coupler is characterized using two-port networks. To obtain the descriptive matrix of the circuit, Figure 5 is divided into six sections, as shown in Figure A.11. Each section is represented by its own two-port network and thus its own descriptive matrix [25]. How to determine these matrices is covered in the following paragraphs.
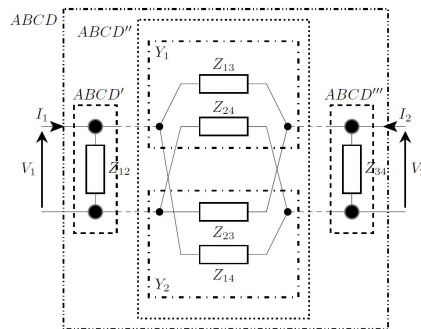

Figure A.11: CPT coupler stripped to its $ABCD$ form

The first two-port in this circuit is, describes the leakage resistance Z_{12} via transformation matrix $ABCD'$. The second two-port, is described by transformation matrix $ABCD''$. This matrix reflects the main and cross coupling

impedances. These impedances have their own admittance matrix, Y_1 and Y_2, respectively. Then these matrices Y_1 and Y_2 are summed to form the admittance matrix Y. Admittance matrix Y is transformed to transformation matrix $ABCD''$. The third transformation matrix $ABCD'''$ describes the leakage resistance at secondary side. The CPT coupler is described by the total transformation matrix $ABCD$, the product of the three transformation matrices $ABCD'$, $ABCD''$ and $ABCD'''$ [25]. The first step is determining admittance matrices Y_1 and Y_2. Figure A.12 represents a general circuit where the components are considered as a black box. The following equations are used to determine the admittance matrices.

$$I_1 = Y_{11} \cdot V_1 + Y_{12} \cdot V_2 \tag{A.1}$$
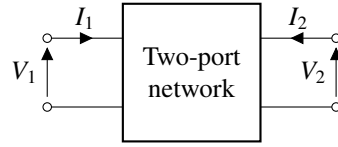$$I_2 = Y_{21} \cdot V_1 + Y_{22} \cdot V_2 \tag{A.2}$$

Figure A.12: General two-port network

Based on these equations, the behavior of impedances Z_{13}, Z_{24}, Z_{23} and Z_{14} in Figure A.11 is described in Equations (A.3) and (A.4).

Admittance matrix Y_1 with impedances Z_{13} and Z_{24}:

$$Y_1 = \begin{bmatrix} \frac{1}{Z_{13}+Z_{24}} & -\frac{1}{Z_{13}+Z_{24}} \\ -\frac{1}{Z_{13}+Z_{24}} & \frac{1}{Z_{13}+Z_{24}} \end{bmatrix} \tag{A.3}$$

Admittance matrix Y_2 with impedances Z_{23} and Z_{14}:

$$Y_2 = \begin{bmatrix} \frac{1}{Z_{23}+Z_{14}} & \frac{1}{Z_{23}+Z_{14}} \\ \frac{1}{Z_{23}+Z_{14}} & \frac{1}{Z_{23}+Z_{14}} \end{bmatrix} \tag{A.4}$$

Because these two networks are in parallel with each other, the two admittances matrices Y_1 and Y_2 are summed resulting in Y.

$$Y = Y_1 + Y_2 = \begin{bmatrix} \frac{Z_{13}+Z_{24}+Z_{23}+Z_{14}}{(Z_{13}+Z_{24})\cdot(Z_{23}+Z_{14})} & \frac{Z_{13}+Z_{24}-Z_{23}-Z_{14}}{(Z_{13}+Z_{24})\cdot(Z_{23}+Z_{14})} \\ \frac{Z_{13}+Z_{24}-Z_{23}-Z_{14}}{(Z_{13}+Z_{24})\cdot(Z_{23}+Z_{14})} & \frac{Z_{13}+Z_{24}+Z_{23}+Z_{14}}{(Z_{13}+Z_{24})\cdot(Z_{23}+Z_{14})} \end{bmatrix} \tag{A.5}$$

Assuming the coupler is symmetric, the impedances Z_{13} to Z_{34} are simplified.

$$Z_{13} = Z_{24} = Z_{main} \tag{A.6}$$
$$Z_{23} = Z_{14} = Z_{cross} \tag{A.7}$$
$$Z_{12} = Z_{34} = Z_{leak} \tag{A.8}$$

Using these assumptions, the admittance matrix Y is simplified.

$$Y = \begin{bmatrix} \frac{Z_{main}+Z_{cross}}{2\cdot Z_{main}\cdot Z_{cross}} & \frac{Z_{main}-Z_{cross}}{2\cdot Z_{main}\cdot Z_{cross}} \\ \frac{Z_{main}-Z_{cross}}{2\cdot Z_{main}\cdot Z_{cross}} & \frac{Z_{main}+Z_{cross}}{2\cdot Z_{main}\cdot Z_{cross}} \end{bmatrix} \tag{A.9}$$

As shown in Figure A.11, the coupler is divided into ABCD parameters. To contribute to this, the admittance matrix Y has to be converted to transformation matrix $ABCD''$. This is done using Equation (A.10).

$$\begin{bmatrix} A & B \\ C & D \end{bmatrix} = \begin{bmatrix} \frac{-Y_{22}}{Y_{21}} & \frac{-1}{Y_{21}} \\ \frac{Y_{21} \cdot Y_{21} - Y_{11} \cdot Y_{22}}{Y_{21}} & \frac{-Y_{11}}{Y_{21}} \end{bmatrix} \tag{A.10}$$

$$\implies ABCD'' = \begin{bmatrix} \frac{Z_{main} + Z_{cross}}{Z_{cross} - Z_{main}} & \frac{2 \cdot Z_{main} \cdot Z_{cross}}{Z_{cross} - Z_{main}} \\ \frac{2}{Z_{cross} - Z_{main}} & \frac{Z_{main} + Z_{cross}}{Z_{cross} - Z_{main}} \end{bmatrix} \tag{A.11}$$

The transformations matrices $ABCD'$ and $ABCD'''$ describe the behavior of the leakage impedance Z_{leak} at the primary and secondary side. Because of the assumed symmetry of the coupler, $ABCD'$ and $ABCD'''$ are equal. Based on Figure A.12, the leakage impedance Z_{leak} is considered as a black box. This system is described by Equations (A.12) - (A.14).

$$V_1 = A \cdot V_2 - B \cdot I_2 \tag{A.12}$$
$$I_1 = C \cdot V_2 - D \cdot I_2 \tag{A.13}$$

$$\implies ABCD' = ABCD''' = \begin{bmatrix} 1 & 0 \\ \frac{1}{Z_{leak}} & 0 \end{bmatrix} \tag{A.14}$$

The behavior of the coupler is described by transformation matrix $ABCD$. The coupler is divided in three separate parts $ABCD'$, $ABCD''$ and $ABCD'''$. The multiplication of these three parts forms the matrix $ABCD$.

$$ABCD = ABCD' \cdot ABCD'' \cdot ABCD''' \tag{A.15}$$

$$= \begin{bmatrix} 1 & 0 \\ \frac{1}{Z_{leak}} & 0 \end{bmatrix} \cdot \begin{bmatrix} \frac{Z_{main} + Z_{cross}}{Z_{cross} - Z_{main}} & \frac{2 \cdot Z_{main} \cdot Z_{cross}}{Z_{cross} - Z_{main}} \\ \frac{2}{Z_{cross} - Z_{main}} & \frac{Z_{main} + Z_{cross}}{Z_{cross} - Z_{main}} \end{bmatrix} \cdot \begin{bmatrix} 1 & 0 \\ \frac{1}{Z_{leak}} & 0 \end{bmatrix} \tag{A.16}$$

$$= \begin{bmatrix} \frac{Zmain + Zcross}{Zcross - Zmain} + \frac{2ZmainZcross}{Zleak(Zcross - Zmain)} & \frac{2ZmainZcross}{Zcross - Zmain} \\ \frac{Zmain + Zcross}{Zleak(Zcross - Zmain)} + \frac{2}{Zcross - Zmain} + \frac{\frac{Zmain + Zcross}{Zcross - Zmain} + \frac{2ZmainZcross}{Zleak(Zcross - Zmain)}}{Zleak} & \frac{Zmain + Zcross}{Zcross - Zmain} + \frac{2ZmainZcross}{Zleak(Zcross - Zmain)} \end{bmatrix} \tag{A.17}$$

To describe the coupler by the pi model, the transformation matrix $ABCD$ is transformed into admittance matrix Y_c. This transformation is done by the following equations:

$$\begin{bmatrix} Y_{11} & Y_{12} \\ Y_{21} & Y_{22} \end{bmatrix} = \begin{bmatrix} \frac{D}{B} & \frac{B \cdot C - A \cdot D}{B} \\ \frac{-1}{B} & \frac{A}{B} \end{bmatrix} \tag{A.18}$$

$$\implies Y_c = \begin{bmatrix} \frac{(Z_{leak} + 2 \cdot Z_{main}) \cdot Z_{cross} + Z_{leak} \cdot Z_{main}}{2 \cdot Z_{cross} \cdot Z_{main} \cdot Z_{leak}} & \frac{-Z_{cross} + Z_{main}}{2 \cdot Z_{main} \cdot Z_{cross}} \\ \frac{-Z_{cross} + Z_{main}}{2 \cdot Z_{main} \cdot Z_{cross}} & \frac{(Z_{leak} + 2 \cdot Z_{main}) \cdot Z_{cross} + Z_{leak} \cdot Z_{main}}{2 \cdot Z_{cross} \cdot Z_{main} \cdot Z_{leak}} \end{bmatrix} \tag{A.19}$$

Based on matrix Y_c, the three admittances, Y_m, Y_{tr} and Y_{rcv}. This allows a pi model to be formed analogues to the earlier model in 2.

$$Y_m = \frac{1}{Z_m} = -Y_{c_{12}} = -Y_{c_{21}} = \frac{-Z_{cross} + Z_{main}}{2 \cdot (-Z_{cross} \cdot Z_{main})} \tag{A.20}$$

$$Y_{tr} = \frac{1}{Z_{tr}} = Y_{c_{11}} + Y_{c_{21}} = \frac{Z_{leak} + Z_{cross}}{Z_{leak} \cdot Z_{cross}} \tag{A.21}$$

$$Y_{rcv} = \frac{1}{Z_{rcv}} = Y_{c_{22}} + Y_{c_{21}} = \frac{Z_{leak} + Z_{cross}}{Z_{leak} \cdot Z_{cross}} \tag{A.22}$$

11

References

[1] A. M. Jawad, R. Nordin, S. K. Gharghan, H. M. Jawad, M. Ismail, Opportunities and challenges for near-field wireless power transfer: A review, Energies 10 (7) (2017) 1022. doi:10.3390/en10071022.
URL http://dx.doi.org/10.3390/en10071022

[2] J. Van Mulders, D. Delabie, C. Lecluyse, C. Buyle, G. Callebaut, L. Van der Perre, L. De Strycker, Wireless power transfer: Systems, circuits, standards, and use cases, Sensors 22 (15) (2022) 5573. doi:10.3390/s22155573.
URL http://dx.doi.org/10.3390/s22155573

[3] C. Lecluyse, B. Minnaert, M. Kleemann, A review of the current state of technology of capacitive wireless power transfer, Energies 14 (18).
doi:10.3390/en14185862.
URL https://www.mdpi.com/1996-1073/14/18/5862

[4] Z. Wang, Y. Zhang, X. He, B. Luo, R. Mai, Research and application of capacitive power transfer system: A review, Electronics 11 (7).
doi:10.3390/electronics11071158.
URL https://www.mdpi.com/2079-9292/11/7/1158

[5] A. P. Hu, C. Liu, H. L. Li, A novel contactless battery charging system for soccer playing robot, in: 2008 15th International Conference on Mechatronics and Machine Vision in Practice, 2008, pp. 646–650. doi:10.1109/MMVIP.2008.4749606.

[6] M. Kim, J. Choi, Design of high-frequency resonant inverter for capacitive wireless power transfer, in: 2020 IEEE 21st Workshop on Control and Modeling for Power Electronics (COMPEL), 2020, pp. 1–7. doi:10.1109/COMPEL49091.2020.9265653.

[7] J. Dai, D. C. Ludois, Single active switch power electronics for kilowatt scale capacitive power transfer, IEEE Journal of Emerging and Selected Topics in Power Electronics 3 (1) (2015) 315–323. doi:10.1109/JESTPE.2014.2334621.

[8] J. Choi, D. Tsukiyama, Y. Tsuruda, J. M. R. Davila, High-frequency, high-power resonant inverter with egan fet for wireless power transfer, IEEE Transactions on Power Electronics 33 (3) (2018) 1890–1896. doi:10.1109/TPEL.2017.2740293.

[9] D. Rozario, N. A. Azeez, S. S. Williamson, Comprehensive review and comparative analysis of compensation networks for capacitive power transfer systems, in: 2016 IEEE 25th International Symposium on Industrial Electronics (ISIE), 2016, pp. 823–829. doi:10.1109/ISIE.2016.7744996.

[10] H. Zhang, C. Zhu, F. Lu, Long-distance and high-power capacitive power transfer based on the double-sided lc compensation: Analysis and design, in: 2019 IEEE Transportation Electrification Conference and Expo (ITEC), 2019, pp. 1–5. doi:10.1109/ITEC.2019.8790595.

[11] S. Choi, G. C. Lim, J.-S. Hong, E. Chung, G. Choe, J.-I. Ha, Compensation network design method for capacitive power transfer system considering coupling variation, in: 2022 IEEE Energy Conversion Congress and Exposition (ECCE), 2022, pp. 1–6. doi:10.1109/ECCE50734.2022.9947582.

[12] Y. Hou, S. Sinha, K. Afridi, Tunable multistage matching network for capacitive wireless power transfer system, in: 2021 IEEE Wireless Power Transfer Conference (WPTC), 2021, pp. 1–4. doi:10.1109/WPTC51349.2021.9457989.

[13] B. Regensburger, S. Sinha, A. Kumar, S. Maji, K. K. Afridi, High-performance multi-mhz capacitive wireless power transfer system for ev charging utilizing interleaved-foil coupled inductors, IEEE Journal of Emerging and Selected Topics in Power Electronics 10 (1) (2022) 35–51. doi:10.1109/JESTPE.2020.3030757.

[14] H. Mahdi, B. Hoff, T. Østrem, Optimal solutions for underwater capacitive power transfer, Sensors 21 (24). doi:10.3390/s21248233.
URL https://www.mdpi.com/1424-8220/21/24/8233

[15] H. Mahdi, B. Hoff, P. G. Ellingsen, T. Østrem, Conformal transformation analysis of capacitive wireless charging, IEEE Access 10 (2022) 105621–105630. doi:10.1109/ACCESS.2022.3210960.

[16] R. Erfani, F. Marefat, A. M. Sodagar, P. Mohseni, Modeling and characterization of capacitive elements with tissue as dielectric material for wireless powering of neural implants, IEEE Transactions on Neural Systems and Rehabilitation Engineering 26 (5) (2018) 1093–1099. doi:10.1109/TNSRE.2018.2824281.

[17] R. Erfani, F. Marefat, A. M. Sodagar, P. Mohseni, Modeling and experimental validation of a capacitive link for wireless power transfer to biomedical implants, IEEE Transactions on Circuits and Systems II: Express Briefs 65 (7) (2018) 923–927. doi:10.1109/TCSII.2017.2737140.

[18] Q. Wang, J. Che, W. Wu, Z. Hu, X. Liu, T. Ren, Y. Chen, J. Zhang, Contributing factors of dielectric properties for polymer matrix composites, Polymers 15 (3) (2023) 590. doi:10.3390/polym15030590.
URL http://dx.doi.org/10.3390/polym15030590

[19] W. Ellison, K. Lamkaouchi, J.-M. Moreau, Water: a dielectric reference, Journal of Molecular Liquids 68 (2) (1996) 171–279.
doi:https://doi.org/10.1016/0167-7322(96)00926-9.
URL https://www.sciencedirect.com/science/article/pii/0167732296009269

[20] H. Xu, B. Li, S. Xu, H. Feng, The measurement of dielectric constant of the concrete using single-frequency cw radar, in: 2008 First International Conference on Intelligent Networks and Intelligent Systems, 2008, pp. 588–591. doi:10.1109/ICINIS.2008.139.

[21] S. S. Zhekov, O. Franek, G. F. Pedersen, Dielectric properties of common building materials for ultrawideband propagation studies [measurements corner], IEEE Antennas and Propagation Magazine 62 (1) (2020) 72–81. doi:10.1109/MAP.2019.2955680.

[22] L. Huang, A. Hu, Defining the mutual coupling of capacitive power transfer for wireless power transfer, Electronics Letters 51 (22) (2015) 1806–1807. arXiv:https://ietresearch.onlinelibrary.wiley.com/doi/pdf/10.1049/el.2015.2709, doi:https://doi.org/10.1049/el.2015.2709.
URL https://ietresearch.onlinelibrary.wiley.com/doi/abs/10.1049/el.2015.2709

[23] E. J. Murphy, S. O. Morgan, The dielectric properties of insulating materials, iii alternating and direct current conductivity, The Bell System Technical Journal 18 (3) (1939) 502–537. doi:10.1002/j.1538-7305.1939.tb03589.x.

[24] B. Minnaert, N. Stevens, Conjugate image theory applied on capacitive wireless power transfer, Energies 10 (1). doi:10.3390/en10010046.
URL https://www.mdpi.com/1996-1073/10/1/46

[25] I. Mayergoyz, W. Lawson, Chapter 10 - magnetically coupled circuits and two-port elements, in: I. Mayergoyz, W. Lawson (Eds.), Basic Electric Circuit Theory, Academic Press, San Diego, 1997, pp. 381–430. doi:https://doi.org/10.1016/B978-0-08-057228-4.50014-8.
URL https://www.sciencedirect.com/science/article/pii/B9780080572284500148

[26] M. Brotherton, CAPACITORS Their Use in Electronics, D. Van Nostrand Company, Inc., 1946.

[27] C. Lecluyse, B. Minnaert, S. Ravyts, M. Kleemann, Influence of a medium on capacitive power transfer capability, in: 2022 Wireless Power Week (WPW), 2022, pp. 589–594. doi:10.1109/WPW54272.2022.9853947.

[28] M. Mehdizadeh, Chapter 1 - the impact of fields on materials at microwave and radio frequencies, in: M. Mehdizadeh (Ed.), Microwave/RF Applicators and Probes (Second Edition), second edition Edition, William Andrew Publishing, Boston, 2015, pp. 1–33. doi:https://doi.org/10.1016/B978-0-323-32256-0.00001-4.
URL https://www.sciencedirect.com/science/article/pii/B9780323322560000014

[29] S. B. Aziz, H. M. Ahmed, Structure, dielectric properties and ac behavior of commercial polytetrafluroethylene (ptfe) polymer, Aro-The Scientific Journal of Koya University 1 (1) (2016) 29–33. doi:10.14500/aro.10033.
URL http://aro.koyauniversity.org/index.php/aro/article/view/ARO.10033

[30] C. Lecluyse, K. Peirens, S. Ravyts, P. Bracke, B. Minnaert, M. Kleemann, Automated test setup for capacitive power transfer coupler impedance measurements, in: 2023 XXXVth General Assembly and Scientific Symposium of the International Union of Radio Science (URSI GASS), 2023, pp. 1–3, to be published.

[31] U. Kaatze, The dielectric properties of water in its different states of interaction, Journal of Solution Chemistry 26 (1997) 1049–1112. doi:10.1007/BF02768829.

[32] U. Kaatze, Techniques for measuring the microwave dielectric properties of materials, Metrologia 47 (2) (2010) S91. doi:10.1088/0026-1394/47/2/S10.

[33] M. Shima, M. Sato, M. Atsumi, K. Hatada, Dipole moments of isotactic and syndiotactic poly(methyl methacrylate) and their temperature dependence, Polymer Journal 26 (5) (1994) 579–585. doi:10.1295/polymj.26.579.

[34] P. G. Huray, S. G. Pytel, R. I. Mellitz, S. H. Hall, Dispersion effects from induced dipoles, in: 2006 IEEE Workship on Signal Propagation on Interconnects, 2006, pp. 213–216. doi:10.1109/SPI.2006.289224.